A&A, 707, A274 (2026)
https://doi.org/10.1051/0004-6361/202558292

Astronomy & Astrophysics

Homogeneous abundance ratios of hydrostatic and explosive α-elements in globular clusters from high-resolution optical spectroscopy*

Eugenio Carretta**

INAF – Osservatorio di Astrofisica e Scienza dello Spazio di Bologna, Via P. Gobetti 93/3, 40129 Bologna, Italy

Received 27 November 2025 / Accepted 24 January 2026

ABSTRACT

Galactic globular clusters (GCs) were born shortly after the Big Bang. For these old stellar systems, the initial mass function (IMF) in the high-mass regime can never be observed directly, because stars more massive than about 1 $M_\odot$ have evolved since for a long time. However, the hydrostatic to explosive α-element ratio (HEx ratio) offers a way to bypass the lack of observable high-mass stars through the yields that massive stars released when they exploded as supernovae, which is incorporated in the stars we currently observe in GCs. The HEx ratio measures the percentage of high-mass stars over the total number of stars exploding as supernovae, and it is an efficient probe of the ephemeral first phases of the GC evolution. We exploited a recently completed survey to assemble a dataset of very homogeneous abundances of α-elements in 27 GCs from [Fe/H] ~ −2.4 to ~−0.3 dex. In agreement with previous results from APOGEE, we confirm that the HEx ratio is indistinguishable for GCs that formed in situ and accreted in the Galaxy, and that this ratio decreases with increasing metallicity. However, we posit that this trend is better explained by a metallicity-dependent IMF that is deficient in the highest-mass stars at high metallicity, as corroborated by the declining [O/Mg] ratio as a function of the [Mg/H] ratio. At odds with the previous analysis based on APOGEE data, we detect an anti-correlation of HEx ratio with both present-day and initial GC masses. Finally, we hypothesise that in the analysis of APOGEE data, the stars of the GC M 54 were probably confused with stars in the core of the Sagittarius dwarf galaxy, in which the cluster is currently immersed.

Key words. stars: abundances – stars: atmospheres – stars: Population II – globular clusters: general

1. Introduction

Oxygen follows hydrogen and helium as the most abundant elements in the Universe. Reactions with successive captures of He nuclei (α particles) on Ne synthetise Mg, Si, Ca, and Ti (e.g. Burbidge et al. 1957), which are collectively known as α-elements. These elements are enhanced in metal-poor stars (see Wallerstein 1962, and in particular, in globular clusters (GCs) of the Milky Way (MW). This occurrence is explained with the interplay between star formation and the lifetime of stars in different mass ranges (Tinsley 1979). Massive stars evolve quickly, leading to a quick (prompt) release of copious amounts of α-elements in core-collapse supernovae (CCSNe), well before the bulk of contribution by type Ia SNe, whose precursors evolve on a longer (delayed) timescale, might lower the [α/Fe][1] ratio by raising the iron content of the yields. The level of α-elements measured in a stellar system is then a probe of the efficiency of the system to produce and retain yields from massive stars before the onset of the bulk of SNe Ia.

However, the dominant nucleosynthetic channels are different for different species belonging to this group. The synthesis of O and Mg is dominated by hydrostatic burning in the outermost shells of the most massive stars (in the range 15–30 $M_\odot$) before being released by CCSNe (e.g. Weinberg et al. 2019 and references therein). As a consequence, they are dependent on the mass of the star, with yields increasing with increasing progenitor mass, but only a weak dependence on metallicity at fixed stellar mass (e.g. Woosley & Weaver 1995; Andrews et al. 2017; Griffith et al. 2019). Explosive α-elements such as Si, Ca, and Ti are produced in shells lying closer to the core of massive stars. This makes their yields relatively independent of stellar mass when they are released by SNe, predominantly by CCSNe, with a lower but significant contribution from SNe Ia (e.g. Nomoto et al. 1984).

These different properties mean that the comparison of α-elements produced in hydrostatic burning (O and Mg) to the abundance of explosive α-elements (Si, Ca, and Ti) is an efficient way to sample the high-mass end of the initial mass function (IMF) of a given stellar population (e.g. McWilliam et al. 2013; Carlin et al. 2018) through the analysis of the yields incorporated in the stars we currently observe. For GCs, this is an important probe because stars more massive than ~1 $M_\odot$ have evolved since for a long time off the main sequence and are difficult to observe.

The first and most straightforward applications of this method were made for the Sagittarius dwarf galaxy (Sgr dSph). Using the [Mg/Ca] ratio as an example of the hydrostatic-to-explosive abundance ratio of α-elements, McWilliam et al. (2013) concluded that the decline of this ratio with increasing metallicity suggests evidence that the IMF is deficient in the highest-mass stars. Carlin et al. (2018), who coined the term

* Based on observations collected at ESO telescopes under programmes (see Appendix).

** Corresponding author: eugenio.carretta@inaf.it

[1] We adopt the usual spectroscopic notation, i.e. [X] = $\log(X)_{star} - \log(X)_\odot$ for any abundance quantity X, and $\log \epsilon(X) = \log(N_X/N_H) + 12.0$ for absolute number density abundances.

HEx ratio, reached a similar conclusion by studying this ratio in 42 stars in the Sgr tidal stream. Both studies were based on optical high-resolution spectroscopy.

The same approach is made more complicated in GCs by the presence of multiple stellar populations (MPs). Whereas most heavy elements show a high degree of homogeneity in GCs (e.g. Gratton et al. 2004), MPs are distinct by variations in the abundances of light elements, modified by proton-capture reactions with respect to the primordial level established in GCs by SNe (see Gratton et al. 2012, 2019 for comprehensive reviews). In the network of proton-capture reactions in H-burning at high temperature (e.g. Langer et al. 1993), the hydrostatic α-elements O and Mg are both consumed to produce N and Al. Oxygen can be depleted even down to [O/Fe] ~ -1 dex starting from the mean enhancement (0.3–0.4 dex) typical of GCs, and its variations are observed in almost every GCs in the MW (e.g. Carretta et al. 2010a). The depletion of the Mg abundances is much more moderate, and significant variations are only observed in GCs that are metal poor, massive, or both (Carretta et al. 2009a; Mészáros et al. 2020). The explosive elements Si and Ca are also affected by the MP phenomenology. In the case of Si, the changes in the abundances are usually small, since the main mechanism is actually a leakage on Si from the Mg-Al cycle (e.g. Arnould et al. 1999; Yong et al. 2005). Variations in Ca, detected as small but observable excesses with respect to unpolluted field stars of similar metallicity, are much more rare and are found in about 10% of all the surveyed GCs (Carretta & Bragaglia 2021).

A large survey of HEx ratios in GCs, as well as in halo substructures and satellites galaxies of the MW, was recently conducted by Horta & Ness (2025; hereinafter HN25), who exploited the APOGEE survey DR17. They used the unpolluted stellar population in GCs and selected N-poor/C-rich and Al-poor/Mg-rich stars. They favoured an alternative scenario that explains the decreasing trend of HEx ratios in GCs with the metallicity with a delayed contribution of SNe Ia, leading to a higher contribution of both iron and explosive α-elements.

We take advantage of a recently completed survey of Mg, Si, Ca, and Ti from high-resolution optical spectroscopy in 16 GCs (Carretta 2026). We describe the available data in Section 2, compute the HEx ratios for GCs in Section 3, and compare our results with those from the APOGEE survey (Section 4). Finally, we discuss and summarise our findings in Section 5.

2. Datasets

We added another 11 GCs studied by the same group in individual papers to the sample in Carretta (2026). The average abundances of oxygen and other α-elements are listed in Table 1 in the first row for each GC, together with the cluster metallicity [Fe/H] on the metallicity scale by Carretta et al. (2009b) from high-resolution UVES spectra. We stress that this ensemble of 27 GCs represents a very homogeneous dataset that was analysed with an identical method. We employed the same scale of atmospheric parameters, the same line list, the same method for measurements of equivalent widths, and the same reference solar abundances. All the stars (more than 2600 with Fe and at least a measured species of α-elements) have their membership certified by radial velocity and abundance. References for all the papers from which the abundances of individual stars can be retrieved (usually in electronic form at CDS) are given in Table A.1.

We adopted the classification given in Massari et al. (2019), with a few amendments as in Carretta (2026), for the birth place of GCs. In our sample, eight GCs are in situ clusters, born in the disc or bulge of the Milky Way. The other objects are thought to have formed in former external systems and to have been brought afterwards into the main Galaxy from the accretion events linked to Gaia-Enceladus, Sequoia, the Helmi streams, Sagittarius, or the group of low orbital energy GCs of still uncertain origin.

We used field stars of the Milky Way as a reference baseline. We employed the sample of stars with good parallaxes by Gratton et al. (2003), from which we also adopted our solar reference abundances. The field stars cover the same metallicity range as spanned by the GC sample, and the abundances were derived from the same line list as used for GC stars. Another reference consisted of 27 stars in the nucleus of the Sgr dSph from Carretta et al. (2010c). Although limited in size, this sample is useful to evaluate the behaviour of the HEx ratio in a substructure accreted in the Milky Way. From the comparison of the abundances, Carretta et al. (2010c) showed that the stars in the Sgr core can be distinct from those of the GC NGC 6715. While currently embedded in the Sgr core, this GC probably formed separately and plunged into the core of Sgr due to dynamical friction only at later times. The different chemistry of core stars and GC is clearly highlighted by proton-capture elements (Carretta et al. 2010c), but it also appears to be shared by the ratio of hydrostatic to explosive α-elements (see below).

The impact of the properties of MPs is a potential problem in deriving the correct or unbiased HEx ratio for GCs. Abundance variations due to proton-capture reactions in H-burning at high temperature in particular affect the hydrostatic species O and Mg, and only to a smaller extent explosive α-elements such as Si and Ca (see e.g. Section 1 and Carretta 2026). This potential bias can be efficiently solved by using only the unpolluted stellar component in GCs, that is, the fraction of stars that still maintained the original chemical composition before the polluters enriched the proto-cluster in ejecta processed by proton-capture reactions.

For this purpose, we adopted the criteria given in Carretta et al. (2009c) for the classification of MPs in GCs according to the Na-O anti-correlation. The unpolluted component with primordial (P) composition includes all stars with an Na abundance between the minimum [Na/Fe] observed in each GC and $[\mathrm{Na/Fe}]_{\mathrm{min}} + 4\sigma$. The polluted stars were separated into fractions with an intermediate (I) and extreme (E) composition according to their position in the Na–O anti-correlation ([O/Na] > -0.9 and [O/Na] < -0.9 dex, respectively). It is relevant for our study that the P stars bear the composition of unpolluted field stars of similar metallicity, inherited essentially from SNe nucleosynthesis, as shown in Fig. 1. In this figure, we plot the average [Na/H] ratios for the P, I, and E components in our sample of GCs, superimposed on a reference sample of field stars from Carretta (2013). The P stars match the locus of the unpolluted stars well. The good correlation between abundances of O and Mg in MPs (p-value $< 1.0 \times 10^{-6}$ in our sample) ensures that the Mg abundances used in the HEx ratio reliably trace the birth-gas composition. We preferred to use the Na-O anti-correlation as a tool for selecting the P stars because its signature is present in the overwhelming majority of GCs, whereas significant Mg variations are biased towards massive and metal-poor GCs only (see Section 1). The average abundances of the P component are listed in the second row in Table 1 for each GC.

3. The HEx ratio

The derived HEx ratios of hydrostatic to explosive α-elements are shown in Fig. 2 as a function of metallicity for our

Table 1. Average abundances of hydrostatic and explosive α-elements.

GC	[O/Fe]			[Mg/Fe]			[Si/Fe]			[Ca/Fe]			[Ti/Fe] I			[Fe/H]	
	n	mean	rms	n	mean	rms	n	mean	rms	n	mean	rms	n	mean	rms	mean	rms
0104	115	+0.152	0.179	147	+0.530	0.076	147	+0.433	0.061	147	+0.315	0.024	146	+0.394	0.036	–0.768	0.054
P only	31	+0.289	0.083	31	+0.533	0.081	31	+0.399	0.058	31	+0.310	0.023	31	+0.394	0.033		
0288	70	+0.132	0.257	107	+0.469	0.045	112	+0.389	0.029	111	+0.402	0.045	106	+0.283	0.040	–1.305	0.054
P only	23	+0.286	0.196	22	+0.465	0.043	23	+0.379	0.035	23	+0.394	0.035	23	+0.270	0.030		
0362	71	+0.091	0.189	87	+0.328	0.042	89	+0.248	0.040	91	+0.334	0.026	86	+0.172	0.037	–1.166	0.048
P only	16	+0.219	0.097	14	+0.347	0.034	15	+0.231	0.027	16	+0.340	0.030	15	+0.161	0.022		
1851	96	+0.002	0.209	123	+0.374	0.036	124	+0.383	0.029	125	+0.324	0.035	122	+0.155	0.053	–1.185	0.068
P only	30	+0.170	0.112	30	+0.393	0.034	29	+0.365	0.029	30	+0.317	0.029	30	+0.144	0.049		
1904	58	+0.078	0.205	57	+0.272	0.040	68	+0.304	0.036	67	+0.276	0.037	66	+0.131	0.042	–1.579	0.033
P only	19	+0.215	0.098	19	+0.276	0.038	19	+0.292	0.039	19	+0.274	0.033	19	+0.141	0.035		
2808	117	+0.001	0.371	139	+0.272	0.156	140	+0.296	0.054	140	+0.328	0.023	140	+0.213	0.033	–1.129	0.030
P only	42	+0.308	0.058	46	+0.384	0.041	46	+0.265	0.026	46	+0.321	0.024	46	+0.215	0.033		
3201	110	+0.125	0.286	131	+0.341	0.049	146	+0.299	0.038	150	+0.306	0.039	118	+0.082	0.037	–1.512	0.065
P only	35	+0.273	0.166	32	+0.338	0.041	35	+0.293	0.039	35	+0.293	0.035	34	+0.079	0.034		
4590	56	+0.403	0.178	62	+0.364	0.066	54	+0.423	0.057	120	+0.280	0.042	18	+0.162	0.048	–2.265	0.047
P only	19	+0.473	0.177	18	+0.350	0.065	13	+0.409	0.049	19	+0.272	0.042	8	+0.164	0.048		
4833	61	+0.243	0.270	52	+0.338	0.173	71	+0.459	0.051	78	+0.351	0.015	62	+0.167	0.023	–2.015	0.014
P only	16	+0.456	0.102	14	+0.508	0.078	16	+0.426	0.027	16	+0.349	0.018	16	+0.166	0.026		
5634	6	+0.292	0.134	7	+0.519	0.032	7	+0.295	0.031	7	+0.299	0.024	7	+0.146	0.015	–1.867	0.050
P only	3	+0.388	0.107	4	+0.512	0.047	4	+0.296	0.045	4	+0.285	0.024	4	+0.137	0.015		
5904	114	+0.139	0.282	135	+0.422	0.052	137	+0.320	0.034	138	+0.371	0.028	133	+0.181	0.027	–1.340	0.052
P only	31	+0.387	0.122	31	+0.418	0.053	31	+0.310	0.037	31	+0.369	0.032	31	+0.182	0.029		
6093	63	+0.223	0.217	70	+0.458	0.061	79	+0.354	0.031	82	+0.356	0.016	68	+0.189	0.029	–1.792	0.023
P only	18	+0.405	0.111	17	+0.461	0.048	17	+0.351	0.037	18	+0.356	0.016	18	+0.187	0.028		
6121	88	+0.218	0.118	104	+0.545	0.045	104	+0.538	0.039	104	+0.415	0.035	104	+0.281	0.033	–1.168	0.046
P only	26	+0.313	0.079	26	+0.547	0.050	26	+0.519	0.039	26	+0.412	0.031	26	+0.277	0.034		
6171	30	+0.172	0.187	33	+0.522	0.044	33	+0.524	0.049	33	+0.415	0.032	33	+0.174	0.038	–1.033	0.064
P only	10	+0.309	0.075	10	+0.533	0.028	10	+0.528	0.056	10	+0.425	0.031	10	+0.170	0.032		
6218	75	+0.281	0.275	81	+0.537	0.037	81	+0.356	0.044	81	+0.420	0.038	80	+0.251	0.024	–1.330	0.042
P only	18	+0.525	0.137	18	+0.540	0.032	18	+0.316	0.034	18	+0.410	0.047	18	+0.254	0.025		
6254	109	+0.271	0.212	129	+0.481	0.065	144	+0.314	0.057	152	+0.342	0.037	130	+0.176	0.043	–1.575	0.059
P only	33	+0.401	0.131	32	+0.519	0.067	31	+0.294	0.051	33	+0.328	0.037	33	+0.166	0.045		
6388	183	–0.071	0.229	184	+0.220	0.052	184	+0.317	0.063	185	+0.067	0.046	185	+0.275	0.096	–0.480	0.045
P only	53	+0.103	0.145	53	+0.233	0.053	53	+0.284	0.048	54	+0.053	0.050	54	+0.258	0.105		
6397	19	+0.274	0.085	97	+0.454	0.041	49	+0.337	0.037	147	+0.290	0.035	38	+0.177	0.037	–1.988	0.044
P only	4	+0.332	0.069	4	+0.467	0.040	4	+0.326	0.037	4	+0.267	0.037	4	+0.164	0.025		
6441	29	+0.040	0.180	29	+0.370	0.130	30	+0.400	0.180	29	+0.170	0.180	27	+0.320	0.180	–0.348	0.090
P only	11	+0.100	0.100	11	+0.410	0.130	11	+0.360	0.210	11	+0.110	0.170	10	+0.250	0.150		
6535	27	+0.602	0.190	24	+0.479	0.051	6	+0.418	0.035	7	+0.312	0.018	7	+0.184	0.036	–1.952	0.036
P only	8	+0.699	0.178	7	+0.495	0.035	7	+0.428	0.048	8	+0.339	0.043	6	+0.186	0.045		
6715	76	+0.070	0.344	75	+0.344	0.170	77	+0.414	0.102	77	+0.363	0.107	77	+0.166	0.137	–1.505	0.164
P only	21	+0.359	0.078	21	+0.421	0.102	21	+0.385	0.081	21	+0.307	0.083	21	+0.095	0.099		
6752	107	+0.242	0.245	125	+0.387	0.107	137	+0.476	0.062	130	+0.397	0.033	134	+0.181	0.039	–1.555	0.051
P only	26	+0.452	0.163	25	+0.457	0.058	26	+0.434	0.064	26	+0.395	0.027	24	+0.174	0.035		
6809	113	+0.251	0.191	129	+0.483	0.061	146	+0.380	0.044	152	+0.363	0.042	133	+0.147	0.056	–1.934	0.063
P only	17	+0.380	0.090	17	+0.523	0.041	17	+0.377	0.041	17	+0.360	0.052	17	+0.140	0.050		
6838	43	+0.364	0.112	51	+0.496	0.043	51	+0.391	0.051	51	+0.312	0.050	51	+0.366	0.070	–0.832	0.061
P only	12	+0.403	0.109	12	+0.499	0.042	12	+0.391	0.056	12	+0.274	0.050	12	+0.342	0.067		
7078	45	+0.308	0.187	55	+0.420	0.175	59	+0.472	0.093	82	+0.273	0.054	36	+0.219	0.040	–2.320	0.057
P only	13	+0.438	0.125	13	+0.542	0.107	10	+0.395	0.081	13	+0.254	0.053	12	+0.213	0.029		
7099	35	+0.376	0.264	33	+0.505	0.044	22	+0.367	0.058	68	+0.323	0.051	24	+0.240	0.032	–2.344	0.049
P only	12	+0.507	0.115	10	+0.511	0.035	5	+0.298	0.062	12	+0.318	0.045	8	+0.234	0.031		
Ter8	6	+0.394	0.045	6	+0.470	0.092	6	+0.248	0.095	6	+0.190	0.038	6	+0.050	0.057	–2.271	0.079
P only	6	+0.394	0.045	6	+0.470	0.092	6	+0.248	0.095	6	+0.190	0.038	6	+0.050	0.057		

Notes. For each GC, the second row lists the average abundances computed using only the P stars with primordial composition. n is the number of stars used in the averages.

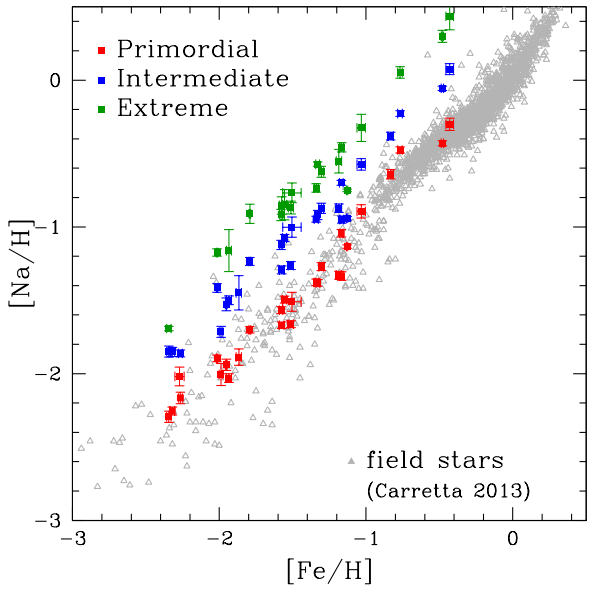

Fig. 1. Average abundance ratio [Na/H] as a function of metallicity for GC stars with primordial (P, red squares), intermediate (I, in blue), and extreme (E, green) composition in our GCs, superimposed on a reference sample of unpolluted field stars from Carretta (2013); open grey triangles.

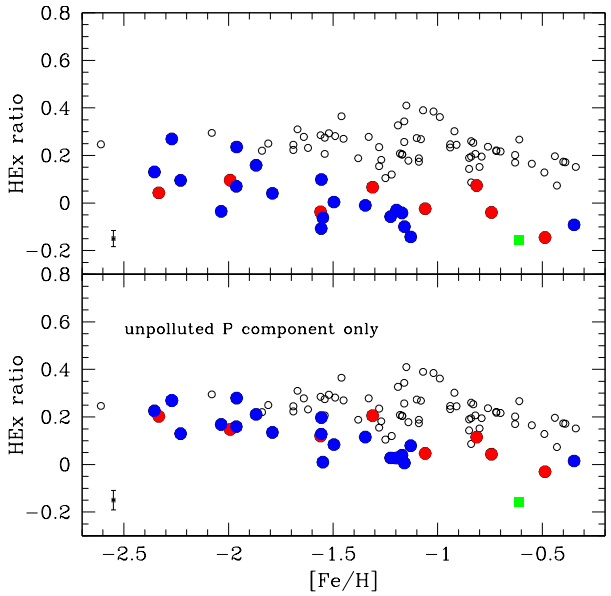

Fig. 2. Ratio of the average of hydrostatic α-elements O and Mg to the average of explosive α-elements Si, Ca, and Ti (HEx ratio) for our sample of GCs. In the lower panel, the ratio is computed using only stars of the unpolluted P component in each GC (see text). The blue and red symbols show accreted and in situ GCs, respectively, and the empty grey circles show field stars from Gratton et al. (2003). The green square shows field stars in the core of Sgr dSph. A typical error is shown in both panels (average from all GCs).

sample of GCs. The ratio was computed from the mean ([O/Fe]+[Mg/Fe])/2 and ([Si/Fe]+[Ca/Fe]+[Ti/Fe])/3 for hydrostatic and explosive species, respectively.

In the upper panel, the averages were made using all stars in GCs, regardless of the P, I, and E class, whereas in the lower panel, we only used the unpolluted P component. The two panels allow us to discern the effect of the MP phenomenon at a glance. In GCs, O can be depleted by as much as 1 dex by proton-capture reactions at moderate temperature (20–40 MK; see e.g. Gratton et al. 2019), whereas the depletion in Mg is usually much smaller, requiring a higher temperature for a significant variation. Compared to the reference field stars, the HEx ratios in the upper panel are lower due to the large depletions in O and the moderate depletions in Mg in the polluted components I and E of GCs. When only the unpolluted component is used (lower panel), the HEx ratios are higher and closer to the locus of field stars.

In both panels, the ratio decreases with increasing [Fe/H], regardless of the origin (in situ or accreted) of GCs. This agrees well with results by HN25 from APOGEE. The HEx ratio for field stars in the Sgr nucleus is located below the plane defined by the GCs, in particular in the lower panel. Again, this is consistent with the overall lower ratio found by HN25 for satellite galaxies when compared to GCs. Field stars (empty circles) seem to show a pattern with a knee at [Fe/H] = –1 dex that is reminiscent of the classical plateau plus a decrease displayed by individual α-elements.

We note that Horta et al. (2020) claimed that a difference exists between the mean level of [Si/Fe] for accreted and in situ subgroups of GCs at metallicity higher than about [Fe/H]=–1.5. However, in HN25 and in our study, there is no dependence on the origin of the various groups of GCs. In the HEx ratio, the weight given to Si is decreased by diluting the relevance of the [Si/Fe] ratio with four other α-elements. These findings apparently corroborate the possible presence of problems in the analysis of Si in APOGEE, as suggested in Carretta (2026).

4. Comparison with APOGEE results

Although the trend with [Fe/H] of the HEx ratio is broadly consistent with the results by HN25 and we agree that in our homogeneous dataset, the locus of accreted and in situ GCs cannot be distinguished, we found a few relevant differences with APOGEE results. First, HN25 claimed that NGC 7078 (M 15) is an outlier, with a low HEx ratio (~0.1) at [Fe/H]~−2.45. In our data, M 15, with a HEx ratio 0.203, is well inside the region populated by the other metal-poor GCs (e.g. NGC 4590, NGC 7099, and Ter 8).

Second, HN25 reported a HEx ratio for NGC 6715 (M 54) that is very close to the value derived for the core of the Sgr galaxy, at [Fe/H] ~ −0.65 dex. This is highly surprising because the average metallicity of M 54 is –1.559[2] (σ = 0.189 dex, 76 stars) according to Carretta et al. (2010c), who also reported a mean [Fe/H] = −0.622 dex from the 27 stars in the Sgr nucleus surrounding M 54. Furthermore, the APOGEE results in Mészáros et al. (2020) give a mean metallicity [Fe/H] = −1.47 (σ = 0.15 dex) for M 54, which is again inconsistent with the value in HN25. To better understand the origin of the discrepancy, we cross-identified the 76 bona fide members of M 54 for radial velocity and abundance in Carretta et al. (2010c) with APOGEE DR17. We found 16 matches, with 6 stars flagged ASPFLAG=0 denoting reliable abundances. Three out of six are unpolluted stars, according to Carretta et al. (2010c). From these, we derived [Fe/H]=–1.482 dex and HEx=+0.140, which agrees very well with the HEx sequence of GCs of similar metallicity. As a check, we next followed the procedure of HN25 by extracting from the value-added catalogue by Schiavon et al. (2024) all entries for NGC6715. We then applied all the selection criteria listed in Section 2 of HN25. The distribution of the metallicities

[2] This value is different from the one in Table 1 because is the average from the larger sample of GIRAFFE stars.

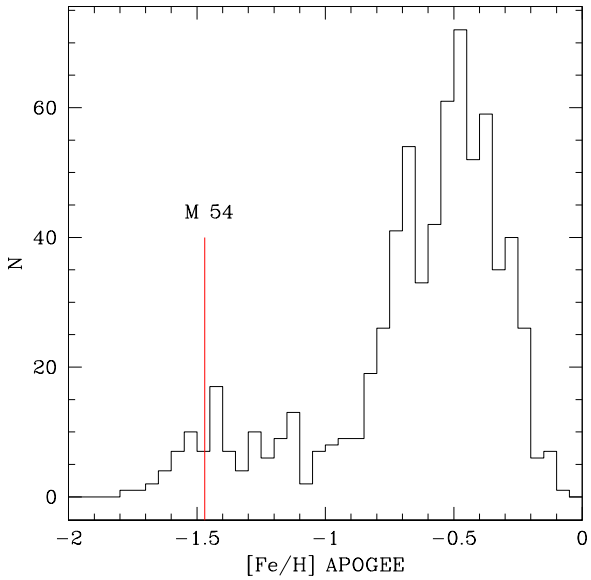

Fig. 3. Distribution of metallicities for stars labelled as candidate members of NGC6715 in Schiavon et al. (2024) after the selection cuts from Horta & Ness (2025). The mean metallicity from APOGEE (Mészáros et al. 2020) for M 54 is indicated by the vertical red line.

from this selection is shown in Fig. 3, where the bulk is at [Fe/H] around –0.6 dex, consistent with the average metallicity for stars in the Sgr nucleus found in Carretta et al. (2010c). In HN25, both M 54 and Sgr seem to be located at this mean value of [Fe/H]. We hypothesise that the selection for the label NGC 6715 probably mostly provided stars of the Sgr core (609 stars), in which the genuine globular cluster M 54 is immersed (the peak at –1.5 dex, 98 stars). The close values shown in HN25 are likely the result of this confusion. The genuine cluster M 54, whose stars show an extended Na-O anti-correlation (signature of a true GC), is much more metal poor (Carretta et al. 2010c; Mészáros et al. 2020). At this metallicity, the hydrostatic and explosive α-elements of its stellar population give a HEx ratio (+0.128 from our analysis) that places M 54 in the midst of the relation defined by GCs, which is clearly distinct from the value (lower HEx ratio and higher metallicity) derived from field stars in the Sgr core (see Fig. 2). Moreover, in our dataset, Terzan 8 (HEx=0.269), another GC associated with the Sgr dSph, is clearly located on the sequence of GCs for its metallicity and is clearly separated from the Sgr field location.

5. Discussion and conclusions

A large survey of α-elements in GCs, recently completed, was exploited together with previous studies to assemble an extremely homogeneous dataset for abundances of hydrostatic and explosive elements in 27 GCs. From this set, we computed the HEx ratio (Carlin et al. 2018) of hydrostatic (O, Mg) to explosive (Si, Ca, and Ti) elements using the primordial P component in GCs to disentangle the original ratios from the effects of MPs that alter predominantly the abundances of O, but also those of Mg, Si, and sometimes Ca (see e.g. Carretta 2026).

In general, despite a few discrepant cases, we confirm with high-resolution optical spectroscopy the main results obtained by HN25 using the near-infrared spectroscopic survey APOGEE. In the plane mapping the HEx ratio as a function of metallicity, the GCs cannot be distinguished by their in situ or accreted origin. In this plane, the sequence of GCs born in the main body of the Milky Way is superimposed on the sequence of GCs that are thought to be formed in external systems. Both sequences lie about 0.1 dex above the locus occupied by satellite galaxies. We had only one comparison represented by stars in the Sgr dSph core for reasons of homogeneity in the abundance analysis. However, this finding is supported by the much larger sample of galaxies and halo substructures shown in HN25.

We also confirmed that the HEx ratios of GCs decrease as the metallicity increases, as shown in HN25. The observed gradient with [Fe/H] can be explained following the two scenarios first discussed by McWilliam et al. (2013) to account for the variation in the [Mg/Ca] ratio over the metallicity range of the Sgr dSph field stars. The HEx ratio measures the contribution to α-elements by hydrostatic burning in massive stars compared to the yield from all the stars exploding as SNe events. The two scenarios affect the numerator and the denominator of the HEx ratio, respectively.

A lower HEx ratio might imply a smaller contribution to the enrichment by the most massive stars ($M > 8$ M$_\odot$) among the SN II progenitors, that is, a top-light (bottom-heavy) IMF like that typical of low-mass satellite galaxies of the Milky Way. This scenario explains the position of dwarf galaxies in the HEx ratio – [Fe/H] plane, which are systematically located at lower HEx ratios than GCs at any metallicity (see HN25, and also the value for Sgr in Fig. 2 of this paper).

Alternatively, a lower HEx ratio might result from changing the factors that control the denominator, for example an excess of type Ia SNe. An increased contribution to the nucleosynthesis as metallicity increases will raise both [Fe/H] and the content of Si, Ca, and Ti, whereas the production of hydrostatic elements is expected to be negligibly low (e.g. Nomoto et al. 1984). This is the explanation preferred by HN25 to account for the trend with metallicity observed for the HEx ratio in GCs.

On the other hand, in a single dSph, Sgr, Carlin et al. (2018) found that the abundance ratios of hydrostatic elements were located much farther below the MW stars used as reference than the abundance ratios of elements produced in explosive nucleosynthesis, suggesting an IMF lacking the most massive SN II progenitors.

It seems to be even more difficult to use a delayed SNe Ia mechanism to explain the decreasing HEx ratio with metallicity for GCs that originated in different environments. The chemodynamics and the age-metallicity relations of GCs in Fig. 2 indicate that they come from five or six galaxies (Massari et al. 2019), that is, the Milky Way disc and bulge, Gaia-Enceladus, Sequoia, Sgr, and the progenitors of the Helmi Stream and low-energy GCs that were later injected into the Milky Way following the accretion events. It is hard to imagine that the SNe Ia contribution worked to place GCs that formed in systems with different global masses, star formation rates, and thus different timescales for the prompt and delayed enrichment from SNe on exactly the same relation as the declining HEx ratio.

The two alternative scenarios can be tested by separately studying the trends with the metallicity of each of the two terms of the HEx ratio, [α_{hydro}/Fe] and [α_{explo}/Fe], as done in Fig. 4. For this figure, we again only employed the average values derived from the primordial P component in each GC to remove the effect of MPs on the ratios. We only adopted Mg as representative of hydrostatic species in field stars to increase the sample size. To better sample the critical region at high metallicity ([Fe/H] $\gtrsim -1$ dex), where the bulk of SNe Ia is expected to manifest, we added GCs from the literature to our sample. We included five bulge GCs and two disc GCs, all with abundances derived from high-resolution optical spectra. The added

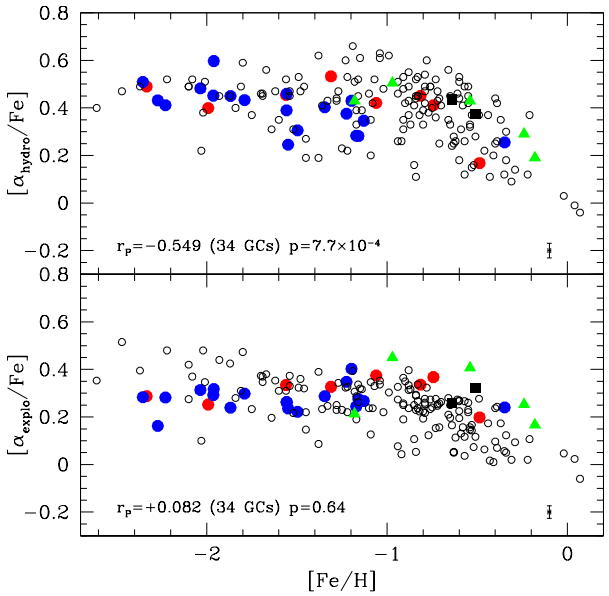

Fig. 4. Abundance ratios of the hydrostatic (upper panel) and explosive (lower panel) α-elements in the GCs of our extended sample. The blue and red points indicate accreted and in situ GCs. The black squares show disc GCs, and the green triangles show bulge GCs from the literature. The Pearson correlation coefficient and two-tailed probability are listed. Only Mg is used to represent the hydrostatic species in field stars.

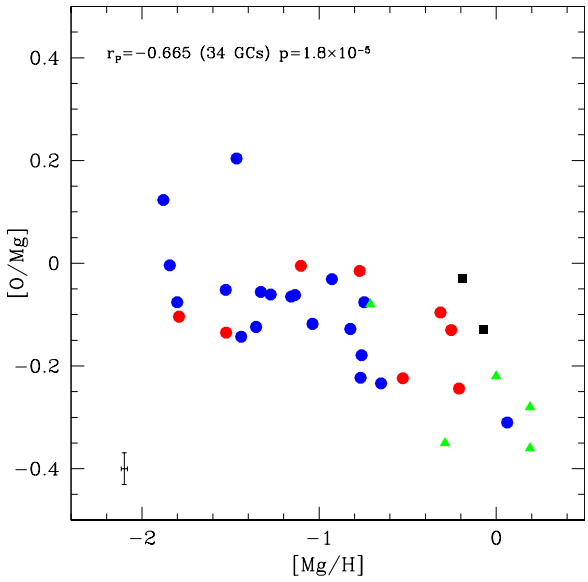

Fig. 5. Abundance ratio [O/Mg] as a function of [Mg/H] for the extended sample of GCs. The symbols are the same as in Fig. 4.

GCs are NGC 6553, NGC 6528, NGC 6440 (Muñoz et al. 2017, 2018, 2020), NGC 6723 (Crestani et al. 2019), NGC 6522 (Barbuy et al. 2021), NGC 5927 (Mura-Guzmán et al. 2018), and NGC 6366 (Puls et al. 2018). All abundances were corrected to our solar abundance scale. Fewer than ten stars are often analysed in these GCs, and we were therefore unable to safely apply the classification by Carretta et al. (2009c) to extract the unpolluted component. However, in these metal-rich GCs, the Na-O anti-correlation has an almost vertical trend (e.g. Muñoz et al. 2020), without a significant spread in O, and the Mg-Al anti-correlation, with significant Mg depletions, is not observed in metal-rich GCs (Carretta et al. 2009a; Mészáros et al. 2020).

We applied a linear regression to the extended sample of GCs in Fig. 4. We list in the panels the Pearson correlation coefficient and the two-tailed probability testing the null hypothesis that the observed value comes from a population in which the true correlation is zero. The lower panel of Fig. 4 shows that the (weak) correlation of the ratio [α_{explo}/Fe] as a function of metallicity is not statistically significant, meaning that the level of explosive α-elements is almost constant in all GCs over the whole metallicity range. Instead, the effect due to the time delay between core-collapse and SNe Ia as detailed by Tinsley (1979) is clearly visible in the reference field stars after about [Fe/H] = –1 dex, in which region stars enter the high-Ia regime. This terminology, adopted from Griffith et al. (2019), is more appropriate to highlight that the ratio in field stars decreases due to the increasing contribution of Fe from SNe Ia, which effectively lowers the plateau established by core-collapse SNe. This lowering is not apparent among GCs, with [α_{explo}/Fe] remaining constant over an interval of about 2 dex in [Fe/H].

Already at low metallicity, the content of hydrostatic species clearly changes with regularity in GCs (upper panel in Fig. 4). The linear regressions listed in Fig. 4 show a statistically significant trend with [Fe/H]. This decline suggests that the effect on the HEx ratio is due to a variation in the properties of the most massive stars (15–30 $M_\odot$).

The irrelevance of contributions from SNe Ia can be better appreciated from Fig. 5, where we plot the ratio [O/Mg] of the elements produced in the hydrostatic cores of massive stars as a function of metallicity. We adopted the ratio [Mg/H] as reference for metallicity because Mg is produced almost entirely by core-collapse SNe, while Fe is provided by SNe II and Ia. For [Mg/H][3], the effect of SN Ia to the enrichment is not contained in this plot (e.g. Gratton et al. 1996, 2000; Fuhrmann 1998).

Even though O and Mg are produced by the same stars on similar timescales, the ratio [O/Mg] is not flat, but decreases with metallicity, and the relation has high statistical significance. The expected yields of hydrostatic elements increase rapidly with progenitor mass (e.g. Woosley & Weaver 1995), and with this strong sensitivity to SN mass, the IMF would affect the abundance ratios. At constant mass, the metallicity dependence is weak (see Andrews et al. 2017), but the IMF-averaged yields might depend on metallicity if the IMF changed as a function of metallicity, which would increase the fraction of low-mass SNe towards higher metallicity (a more top-light IMF). The decline in [O/Mg] with increasing [Mg/H] would then preferentially be explained by a deficit in the highest-mass stars for the more metal-rich GC population.

Several studies have indicated a metallicity-dependent IMF for GCs. For instance, Marks et al. (2012) found that the lower the cluster metallicity, the more top heavy the IMF must have been because the high-mass IMF slope is required to be linearly correlated with metallicity in order to remove residual gas from the proto-GC shortly after the initial star formation. The same conclusion was reached by Wirth et al. (2022) with analytical models tailored to investigate the observed iron spreads in GCs. These authors found that the IMFs of all GCs were more top-heavy than the canonical one, and that a lower metallicity decreases the high-mass slope and makes the GC more top-heavy. The HEx and [O/Mg] ratios, declining with increasing metallicity, support these studies and agree with a scenario in which an IMF that lacks more and more massive stars as [Fe/H] increases, with no compelling need of a significant contribution of Type Ia supernova pre-enrichment.

[3] Our results would be the same for [O/H] instead.

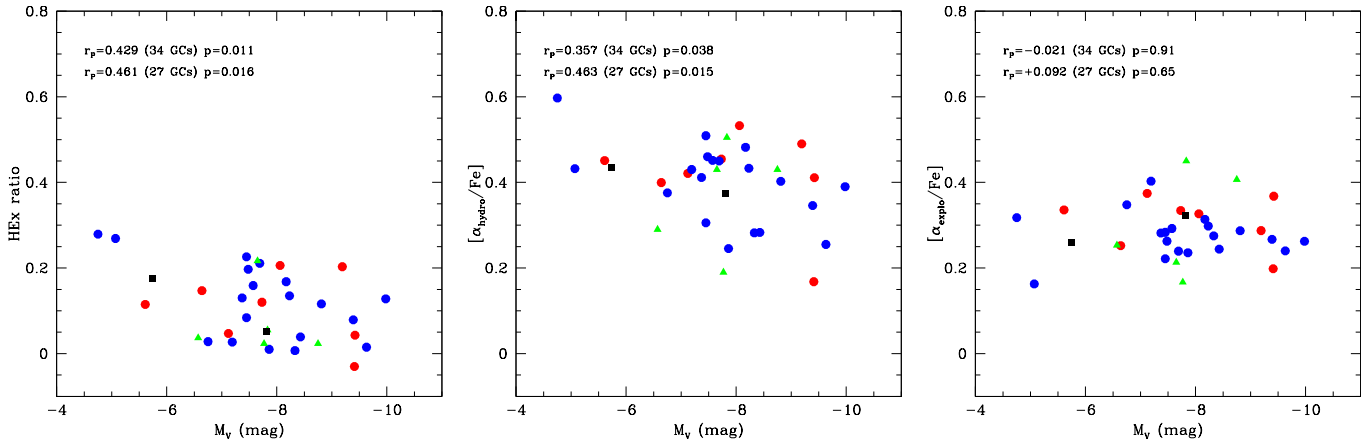

Fig. 6. HEx ratio (left panel), [α_{hydro}/Fe] (middle panel), and [α_{explo}/Fe] ratio (right panel) as a function of the global absolute luminosity of GCs (Harris 2010). The results of the linear regression refer to the extended sample (upper row) and to our original sample (lower row). The symbols are the same as in Fig. 4.

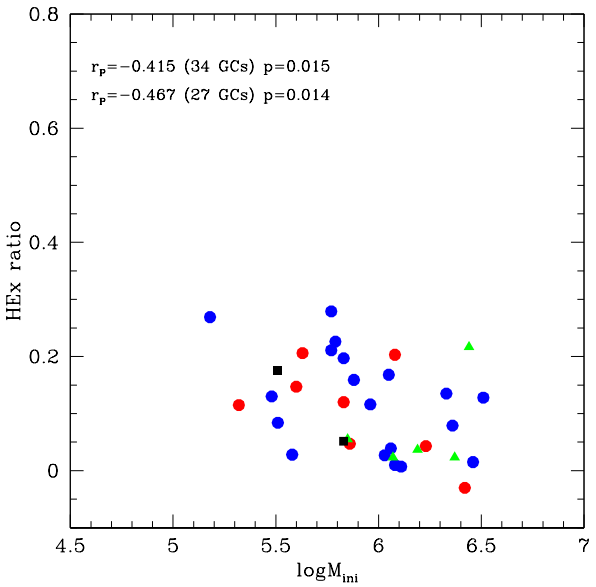

Fig. 7. HEx ratio as a function of the initial GC mass from Baumgardt et al. (2019). The symbols are the same as in Fig. 4.

Finally, at odds with HN25, we found a statistically significant relation between the HEx ratio and the total present-day mass of GCs, using as proxy the total absolute luminosity (Fig. 6, left panel), with the ratio decreasing for higher-mass GCs. The regression is significant using our extended sample (upper row label in the panel) and our original sample of GCs. Again, this correlation is only due to the variation in the content of the elements produced in hydrostatic burning (middle panel in Fig. 6), whereas the [α_{explo}/Fe] ratio remains constant (right panel).

Present-day masses cannot be the best choice for objects like GCs, which formed in a variety of different environments and were subjected to the effects of dynamical evolution for almost a Hubble time. However, the relation between the HEx ratio and the mass appears to be imprinted since the epoch of the GC formation. We found a statistically significant decrease in the HEx ratio also as a function of increasing initial GC masses (estimated by Baumgardt et al. 2019), as shown in Fig. 7, again in contrast with results from HN25, who reported no correlation with GC mass.

We speculate that the decline with total mass might be a reflection of the weak correlation between mass and metallicity among GCs. The most massive objects are preferentially closer to the central regions of the Galaxy, where it is more probable to find metal-rich objects (see e.g. the univariate correlations in Figure 5 of Baumgardt et al. 2019).

To summarise, all the signatures we found (the declining ratio [O/Mg] as a function of [Mg/H], the decreasing HEx ratio with increasing metallicity and with the initial and present-day mass of GCs) would seem to support a coherent picture in which an IMF that changes with metallicity can explain the observed correlations. Even though the IMF in the high-mass regime can never be directly observed in present-day GCs, the content of different α-elements incorporated in the stars we can access today can be efficiently used to probe the ephemeral first phases of GC evolution.

Acknowledgements. This research has made large use of the SIMBAD database (in particular Vizier), operated at CDS, Strasbourg, France, of the NASA's Astrophysical Data System, and TOPCAT (Taylor 2005). I especially thanks Angela Bragaglia and Donatella Romano for several valuable suggestions. I also acknowledge funding from Bando Astrofisica Fondamentale INAF 2023 (PI: A. Vallenari) and from Prin INAF 2019 (PI: S. Lucatello).

References

Andrews, B. H., Weinberg, D. H., Schonrich, R., & Johnson, J. A. 2017, ApJ, 835, 224
Arnould, M., Goriely, S., & Jorissen, A. 1999, A&A, 347, 572
Barbuy, B., Cantelli, E., Muniz, L., et al. 2021, A&A, 654, A29
Baumgardt, H., Hilker, M., Sollima, A., & Bellini, A. 2019, MNRAS, 482, 5138
Bragaglia, A., Carretta, E., D'Orazi, V., et al. 2017, A&A, 607, A44
Burbidge, E. M., Burbidge, G. R., Fowler, W. A., & Hoyle, F. 1957, Rev. Mod. Phys., 29, 547
Carlin, J. L., Sheffield, A. A., Cuhna, K., & Smith, V. V. 2018, ApJ, 859, L10
Carretta, E. 2013, A&A, 557, A128
Carretta, E. 2015, ApJ, 810, 148
Carretta, E. 2026, A&A, in press https://doi.org/10.1051/0004-6361/202558153
Carretta, E., & Bragaglia, A. 2021, A&A, 646, A9
Carretta, E., & Bragaglia, A. 2022, A&A, 659, A122
Carretta, E., & Bragaglia, A. 2023, A&A, 677, A73
Carretta, E., Bragaglia, A., Gratton, R. G., et al. 2007a, A&A, 464, 939
Carretta, E., Bragaglia, A., Gratton, R. G., Lucatello, S., & Momany, Y. 2007b, A&A, 464, 927
Carretta, E., Bragaglia, A., Gratton, R. G., & Lucatello, S. 2009a, A&A, 505, 139
Carretta, E., Bragaglia, A., Gratton, R. G., D'Orazi, V., & Lucatello, S. 2009b, A&A, 508, 695

Carretta, E., Bragaglia, A., Gratton, R. G., et al. 2009c, A&A, 505, 117
Carretta, E., Bragaglia, A., Gratton, R. G., et al. 2010a, A&A, 516, 55
Carretta, E., Bragaglia, A., Gratton, R. G., et al. 2010b, ApJ, 712, L21
Carretta, E., Bragaglia, A., Gratton, R. G., et al. 2010c, A&A, 520, 95
Carretta, E., Lucatello, S., Gratton, R. G., Bragaglia, A., & D'Orazi, V. 2011, A&A, 533, 69
Carretta, E., Bragaglia, A., Gratton, R. G., Lucatello, S., & D'Orazi, V. 2012, ApJ, 750, L14
Carretta, E., Gratton, R. G., Bragaglia, A., D'Orazi, V., & Lucatello, S. 2013a, A&A, 550, A34
Carretta, E., Bragaglia, A., Gratton, R. G., et al. 2013b, A&A, 557, A138
Carretta, E., Bragaglia, A., Gratton, R. G., et al. 2014a, A&A, 564, A60
Carretta, E., Bragaglia, A., Gratton, R. G., et al. 2014b, A&A, 561, A87
Carretta, E., Bragaglia, A., Gratton, R. G., et al. 2015, A&A, 578, A116
Carretta, E., Bragaglia, A., Lucatello, S., et al. 2017, A&A, 600, A118
Crestani, J., Alves-Brito, A., Bono, G., Puls, A. A., & Alonso-Garcia, J. 2019, MNRAS, 487, 5463
Fuhrmann, K. 1998, A&A, 338, 161
Gratton, R., Carretta, E., Matteucci, F., & Sneden, C. 1996, ASPC, 92, 307
Gratton, R., Carretta, E., Matteucci, F., & Sneden, C. 2000, A&A, 358, 671
Gratton, R. G., Carretta, E., Claudi, R., Lucatello, S., & Barbieri, M. 2003, A&A, 404, 187
Gratton, R. G., Sneden, C., & Carretta, E. 2004, ARA&A, 42, 385
Gratton, R. G., Lucatello, S., Bragaglia, A., et al. 2006, A&A, 455, 271
Gratton, R. G., Lucatello, S., Bragaglia, A., et al. 2007, A&A, 464, 953
Gratton, R. G., Carretta, E., & Bragaglia, A. 2012, A&ARv, 20, 50
Gratton, R. G., Bragaglia, A., Carretta, E., et al. 2019, A&ARv, 27, 8
Griffith, E., Johnson, J. A., & Weinberg, D. H. 2019, ApJ, 886, 84
Harris, W. E. 2010, arXiv e-prints [arXiv:1012.3224]
Horta, D., & Ness, M. K. 2025, MNRAS, 544, L64
Horta, D., Schiavon, R. P., Mackereth, J. T., et al. 2020, MNRAS, 493, 3363
Langer, G. E., Hoffman, R., & Sneden, C. 1993, PASP, 105, 301
Marks, M., Kroupa, P., Dabringhausen, J., & Pawlowski, M. S. 2012, MNRAS, 422, 2246
Massari, D., Koppelman, H. H., & Helmi, A. 2019, A&A, 630, L4
McWilliam, A., Wallerstein, G., & Mottini, M. 2013, ApJ, 778, 149
Mészáros, S., Masseron, T., García-Hernández, D. A., et al. 2020, MNRAS, 492, 1641
Muñoz, C., Villanova, S., Geisler, D., et al. 2017, A&A, 605, A12
Muñoz, C., Geisler, D., Villanova, S., et al. 2018, A&A, 620, A96
Muñoz, C., Villanova, S., Geisler, D., et al. 2020, MNRAS, 492, 3742
Mura-Guzmán, A., Villanova, S., & Muñnoz, C. 2018, MNRAS, 474, 4541
Nomoto, K., Thielemann, F.-K., & Yokoi, K. 1984, ApJ, 286, 644
Puls, A. A., Alves-Brito, A., Campos, F., Dias, B., & Barbuy, B. 2018, MNRAS, 476, 690
Schiavon, R. P., Phillips, S. G., Myers, N., et al. 2017, MNRAS, 528, 1393
Taylor, M. B. 2005, Astron. Data Anal. Softw. Syst. XIV, 347, 29
Tinsley, B. M. 1979, ApJ, 229, 1046
Wallerstein, G. 1962, ApJS, 6, 407
Weinberg, D. H., Holtzman, J. A., Hasselquist, S., et al. 2019, ApJ, 874, 102
Wirth, H., Kroupa, P., Haas, J., et al. 2022, MNRAS, 516, 3342
Woosley, S. E., & Weaver, T. A. 1995, ApJS, 101, 181
Yong, D., Grundahl, F., Nissen, P. E., Jensen, H. R., & Lambert, D. L. 2005, A&A, 438, 875

Appendix A: References for the data on globular clusters

In the following table we provide a synopsis of all the papers where the original data on abundances can be retrieved for individual stars in GCs, usually in electronic form at CDS.

Table A.1. References for GC abundances used in this work

GC	[O/Fe]	[Mg/Fe]	[Si/Fe]	[Ca/Fe]	[Ti/Fe] I	[Fe/H]
0104	1,2	2,3	2,3	4,5	5	6
0288	1,2	2,5	2,5	4,5	5	6
0362	7	7	7	7	7	7
1851	8	8	8	8	8	8
1904	1,2	2,5	2,5	4,5	5	6
2808	9	9	9	9	9	9
3201	1,2	2,5	2,5	4,5	5	6
4590	1,2	2,5	2,5	4,5	5	6
4833	10	10	10	10	10	10
5634	11	11	11	11	11	11
5904	1,2	2,5	2,5	4,5	5	6
6093	12	12	12	12	12	12
6121	1,2	2,3	2,3	4,5	5	6
6171	1,2	2,5	2,5	4,5	5	6
6218	2,13	2,5	2,5	4,5	5	6
6254	1,2	2,5	2,5	4,5	5	6
6388	14	14	14	14	14	15
6397	1,2	2,5	2,5	4,5	5	6
6441	16	16	16	16	16	16
6535	17	17	17	17	17	17
6715	18	18	18	18	18	18
6752	2,19	2,20	2,20	4,5	5	6
6809	1,2	2,5	2,5	4,5	5	6
6838	1,2	2,5	2,5	4,5	5	6
7078	1,2	2,5	2,5	4,5	5	6
7099	1,2	2,5	2,5	4,5	5	6
Ter8	21	21	21	21	21	21

- 1=Carretta et al. (2009a), 2=Carretta et al. (2009c), 3=Carretta et al. (2013a)
- 4=Carretta et al. (2010b), 5=Carretta (2026, in press), 6=Carretta et al. (2009b)
- 7=Carretta et al. (2013b), 8=Carretta et al. (2011), 9=Carretta (2015)
- 10=Carretta et al. (2014a), 11=Carretta et al. (2017), 12=Carretta et al. (2015)
- 13=Carretta et al. (2007a), 14=Carretta & Bragaglia (2023), 15=Carretta & Bragaglia (2022)
- 16=Gratton et al. (2006, 2007), 17=Bragaglia et al. (2017), 18=Carretta et al. (2010c)
- 19=Carretta et al. (2007b), 20=Carretta et al. (2012), 21=Carretta et al. (2014b)
- Based on observations collected at ESO telescopes under programmes 072.D-0507, 073.D-0211, 073.D-0.760, 081.D-286, 381.D-0329, 083.D-0208, 085.D-0205, 087.B-0086, 093.B-0.583, 095.D-0834, 099.D-0047.